Geophysical Research Letters

RESEARCH LETTER
10.1029/2019GL085956

Key Points:
- The geometry of surface melt ponds affects the spatial heterogeneity of instantaneous solar irradiance under sea ice
- We define a metric to capture statistics of the sub-ice light field as a function of pond geometry
- We explore the impact of changing surface geometry on under-ice primary production and sea ice melting

Supporting Information:
- Supporting Information S1

Correspondence to:
C. Horvat,
horvat@brown.edu

Citation:
Horvat, C., Flocco, D., ReesJones, D. W., Roach, L. A., & Golden, K. M. (2020). The effect of melt pond geometry on the distribution of solar energy under first-year sea ice. *Geophysical Research Letters*, *47*, e2019GL085956. https://doi.org/10.1029/2019GL085956

Received 29 OCT 2019
Accepted 3 FEB 2020
Accepted article online 6 FEB 2020

©2020. American Geophysical Union. All Rights Reserved.

The Effect of Melt Pond Geometry on the Distribution of Solar Energy Under First-Year Sea Ice

C. Horvat[1], D. Flocco[2,3], D. W. Rees Jones[4,5,6], L. Roach[7], and K. M. Golden[8]

[1]Institute at Brown for Environmental and Society, Brown University, Providence, RI, USA, , [2]National Center for Atmospheric Science, Reading, UK, [3]Centre for Polar Observation and Modelling, University of Reading, Reading, UK, [4]Department of Earth Sciences, University of Oxford, Oxford, UK, [5]Bullard Laboratories, Department of Earth Sciences, University of Cambridge, Cambridge, UK, [6]School of Mathematics and Statistics, University of St Andrews, Saint Andrews, UK, [7]Department of Atmospheric Sciences, University of Washington, Seattle, WA, USA, [8]Department of Mathematics, University of Utah, Salt Lake City, UT, USA

Abstract Sea ice plays a critical role in the climate system through its albedo, which constrains light transmission into the upper ocean. In spring and summer, light transmission through sea ice is influenced by its iconic blue melt ponds, which significantly reduce surface albedo. We show that the geometry of surface melt ponds plays an important role in the partitioning of instantaneous solar radiation under sea ice by modeling the three-dimensional light field under ponded sea ice. We find that aggregate properties of the instantaneous sub-ice light field, such as the enhancement of available solar energy under bare ice regions, can be described using a new parameter closely related to pond fractal geometry. We then explore the influence of pond geometry on the ecological and thermodynamic sea ice processes that depend on solar radiation.

1. Introduction

Solar radiation is a major source of energy in polar regions and is the main driver of growth and melting of sea ice in the Arctic ocean (Perovich & Richter-Menge, 2009). The Arctic sea ice cover is heterogeneous, a mosaic of individual floes that range in size from meters to tens of kilometers. The emergent properties of small-scale sea ice surface variability, in particular the sea ice albedo, are important components of large scale numerical climate models.

Over the course of the melt season, ponds of melt water develop on surface of Arctic sea ice and constitute a significant fraction of the sea ice area, particularly for first-year sea ice (Fetterer & Untersteiner, 1998; Polashenski et al., 2012, 2017; Rösel et al., 2012). Their geometry becomes more complex, with a transition in fractal dimension as pond area grows (Hohenegger et al., 2012).

Because of the high albedo of bare sea ice, changes to the sea ice surface can significantly increase the solar flux to the upper ocean (Perovich et al., 2007). Low-albedo ponds reduce the aggregate albedo of ice-covered areas, increasing solar energy absorbed in and transmitted through the sea ice (Frey et al., 2011; Langleben, 1969; Nicolaus et al., 2012). Arctic surface melt onset has trended toward earlier months in recent decades (Stroeve et al., 2014; Schröder et al., 2014), closer to the peak of the annual solar energy cycle, increasing solar energy input to the Arctic Ocean (Perovich et al., 2007). Locally, enhanced solar radiation below newly formed ponds can enhance sea ice basal melting and further increase solar heating of the upper ocean (Fetterer & Untersteiner, 1998; Perovich et al., 2007). This heat is of critical importance for understanding the seasonal and interannual evolution of the sea ice cover (Perovich et al., 2007). Thinner, more readily ponded first-year ice can transmit much more solar radiation to the upper ocean than multiyear ice (Nicolaus et al., 2012).

Inhomogeneous transmission of solar energy through ponded sea ice leads to an inhomogenous instantaneous under-ice light field at the pond scale (Katlein et al., 2014, 2016). Observations of the under-ice light field in the presence of ponds demonstrate robust, instantaneous sub-ice solar radiation maxima directly under regions of bare sea ice. This effect is a consequence of the inhomogeneous scattering of the light field through the sea ice (Frey et al., 2011; Katlein et al., 2014, 2016).

Sunlight is the primary energy source for phytoplankton, and therefore, instantaneous inhomogeneity in under-ice light may have effects on ocean ecology. Changes to the sea ice surface are likely responsible for an increase in blooms occurring in the early melt season under the ice, in regions of high-concentration ice away from the ice edge (Arrigo et al., 2012, 2014; Assmy et al., 2017; Horvat et al., 2017; Mundy et al., 2009). Evidence for such a shift is seen in measurements of atmospheric iodine, a proxy for under-ice phytoplankton activity (Ordóñez et al., 2012), in a Greenland ice core (Cuevas et al., 2018). An understanding of the evolving light field under-ice is necessary to understand the future of Arctic phytoplankton.

Observational and modeling studies have investigated the transmission and absorption of solar radiation through ponded, bare, first-year, and mixed regions of sea ice (Lu et al., 2008; Light et al., 2008; 2015; Laney et al., 2014, 2017; Nicolaus et al., 2012; Taskjelle et al., 2017). Another investigated relationships between sensor geometry and the 3-D light field under simple regions of mixed water, ice, and ponds (Katlein et al., 2016). Here, we investigate the statistical relationship between the under-ice light field and variations in the pond surface geometry, under a fixed region of thin, ponded, first-year sea ice. In section 2, we describe a method for generating synthetic pond geometries and model the three-dimensional light field below these surfaces. In section 3, we examine statistical features of the under-ice light field for a synthetic data set of 5,000 ponded ice surfaces, demonstrating that the partitioning of solar energy is determined by the overlying pond geometry. In section 4, we explore how pond geometry affects under-ice primary production and sea ice evolution.

2. Methods

2.1. Generation of Synthetic Pond Surfaces

We use synthetic pond surfaces to investigate the statistics of the under-ice light field, allowing us to generate a large number of pond surface configurations with controlled statistical properties. The code to produce these pond surfaces and perform all computations in this study is publicly available as a github repository (supporting information S1). A surface is created by imposing a uniform lattice of individual circular "pseudo-ponds" of radius r^* and total pond fraction ϕ^*, defining a spacing between successive pond centers, $L^2 \approx \pi(r^*)^2/\phi^*$. The positions and radii of individual ponds are perturbed by white noise with a magnitude equal to $2r^*$ and $2L$, respectively. Through this perturbation procedure, the initially circular and separate ponds overlap and form noncircular networks with a total pond fraction $\phi \neq \phi^*$. To isolate the effect of pond geometry, we do not include open water areas, although this would increase the horizontal variance in the under-ice light field.

Figure 1a shows a synthetic ponded sea ice layer using $r^* = 1$ m and $\phi^* = 0.3$, with a pond fraction $\phi = 0.52$. The ice layer is 1 m thick, subject to a solar forcing of 350 W/m^2. The surface is 500 m × 500 m at a resolution of 1 m (dark blue areas are ponded; white areas are unponded). Values are the downwelling planar irradiance (DPI) at the ice-ocean interface.

For each synthetic ponded surface, we use an edge detection algorithm to identify all individual (noncircular) ponds. Indexing the collection of ponds with i, each has a perimeter P_i and area A_i. Across all ponds in an image, the relationship between pond perimeter and area scales with a fractal dimension, D_i, according to

$$P_i \propto (\sqrt{A_i})^{D_i}. \tag{1}$$

We plot the relationship between perimeter and area for all individual ponds as blue circles in Figure 1d and note that an estimate of the fractal dimension of ponds of a certain size is twice the local slope of the $(\log P_i, \log A_i)$ scatter plot in Figure 1d. A statistical method for obtaining a best fit function $D(A)$ for the dependence of pond fractal dimension D on pond area A for a collection of data $(\log P_i, \log A_i)$ is obtained in Bowen et al. (2018). Analysis of thousands of high-resolution ponded sea ice images taken in helicopter-borne surveys displays a transition in $D(A)$ from $D = 1$ to about $D = 2$ as pond area increases, with the transitional regime centered around 100 m^2 (Hohenegger et al., 2012; Huang et al., 2016). Dashed lines in Figure 1d show the slopes corresponding to $D = 1$ (red) and $D = 2$ (yellow) and reproduce the observed transition regime, with results consistent with other methods of pond surface generation (Bowen et al., 2018; Ma et al., 2019; Popović et al., 2018). Thus, our method of pond generation is geometrically realistic.

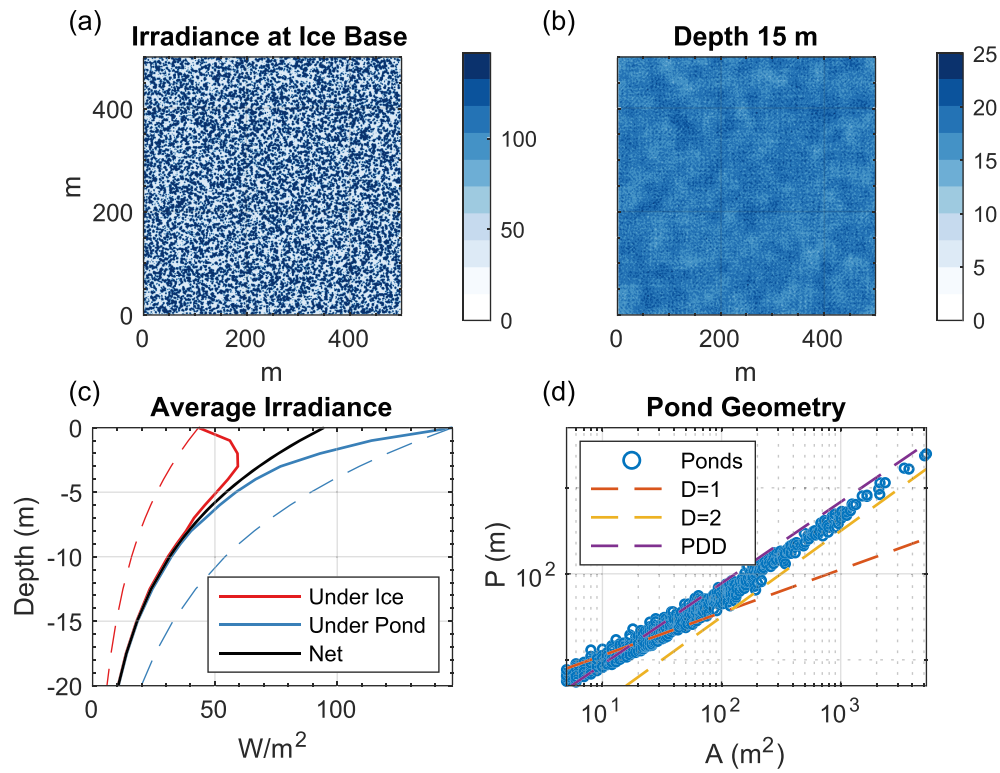

Figure 1. Statistics of a light field under a synthetically generated ponded ice surface. (a) Downwelling planar irradiance (W/m^2) at the ice-ocean interface. (b) Downwelling planar irradiance 15 m below the ice-ocean interface. Note the changed color scale from (a) to (b). (c) Downwelling planar irradiance as a function of depth for (blue) ponded regions, (red) unponded regions, and (black) all. Dashed lines indicate the expected decay profile for a homogenous surface of all ponds or no ponds. (d) Relationship between pond perimeter and pond area for all connected ponds in (a) (blue circles), with slopes corresponding to a fractal dimension of 1 (red dashed line), 2 (yellow dashed line), or the PDD = 1.5 (purple dashed line). The "pond distribution dimension" (PDD) is discussed in section 2.3.

2.2. Under-Ice Light Field Calculation

The solar irradiance at the ice-ocean interface $I_{i/p}$ (units W/m^2, with the subscript i corresponding to bare ice, and p to ponded ice) is assumed to follow

$$I_{i/p} = SWI_{0,i/p}(1 - \alpha_{p/i})\exp(-\kappa_{i/p}H). \tag{2}$$

We take $SW = 350$ W/m^2 to be a representative downwelling solar irradiance in the July Arctic (Kanamitsu et al., 2002; Vihma, 2014). The albedo of the sea ice surface varies in time as it melts because of its surface scattering layer (Grenfell & Maykut, 1977). We choose representative values of $\alpha_i = 0.7$, $\alpha_p = 0.25$, $\kappa_i = 1$, and $\kappa_p = 0.7$ m^{-1}, $H = 1$m, $I_{0,i} = 0.4$, and $I_{0,p} = .75$ for, respectively, the albedoes of bare and ponded ice, the extinction coefficients of bare and ponded ice, ice thickness, and fraction of solar irradiance penetrating the surface scattering layer of bare and ponded melting ice (Grenfell et al., 2006; Light et al., 2008). We follow the approach of Katlein et al. (2016), motivated by the observations of Katlein et al. (2014) and Trodahl et al. (1987), and assume that the light field through a summer ice cover is well characterized by a downward-biased radiance distribution independent of solar angle.

In this idealized model of light transmission through sea ice we assume that ponds have a constant depth. We focus on the horizontal variability in instantaneous light field and not its temporal evolution. Variations in the magnitude of the downwelling solar radiation reaching the sea ice base are accounted for in Delta-Eddington parameterizations of light transfer in climate models (Briegleb & ight, 2007; Holland et al., 2012; Lenoble, 1985). Changes in ice/pond thickness, surface albedo, pond drainage, and refreezing can affect the magnitude of solar radiation penetrating ice and pond surfaces and therefore being absorbed within the water column. In the supporting information Figure S1 we perform a sensitivity experiment that assumes no surface scattering layer ($I_{0,i} = I_{0,p} = 1$) and the same extinction coefficient under-ice and ponds

($\kappa_i = \kappa_p = 0.7\ \mathrm{m}^{-1}$). These changes to sea ice properties alter the total and relative fluxes of solar energy through pond and ice surfaces but give similar results to what follows below.

We calculate the three-dimensional under-ice light field using the (Katlein et al., 2016) ray optical radiative transfer model, which calculates the DPI in the ocean below sea ice given the DPI at the ice base from equation (2). We compute the DPI by integrating over all rays reaching a given ocean point from the surface, assuming an anisotropic radiance distribution (Katlein et al., 2014; Trodahl et al., 1987) at the ice base and that light is attenuated following Beer's law with an extinction coefficient of $\kappa_w = 0.11\ \mathrm{m}^{-1}$. Following Katlein et al. (2016), we assume no scattering within the ocean, a suitable approximation for clear under-ice Arctic waters, although the presence of biology could increase both scattering and attenuation of light with depth. We perform the light calculation for each point in the ocean, using a doubly periodic domain so that there are no edge effects.

Figure 1c shows statistics of the under-ice light field for the pond surface in Figure 1a. The average planar irradiance (Figure 1c, black line) decays exponentially with a decay length scale $\kappa_w^{-1} = 9$ m, yet as a consequence of the inhomogenous distribution of light penetrating sea ice, the average planar irradiance under ponded ice (Figure 1c, blue line) or pond-free ice (Figure 1c, red line) does not follow an exponential decay profile (dashed lines, Figure 1c). Instead, the initially heterogeneous light field becomes more homogeneous at depth (Figure 1b). In pond-free areas, there is a significant increase in solar irradiance up to a depth of several meters (Frey et al., 2011).

For the melt pond surface shown in Figure 1a with a pond area fraction, $\phi = 0.52$, a domain-wide average of 100 W/m^2 of solar energy penetrates the sea ice base (black line at $z = 0$, Figure 1c), with 70 W/m^2 absorbed in the top 10 m. Per square meter of sea ice surface, most of that solar energy (80 W/m^2, blue lines at $z = 0$, Figure 1c) penetrates ponded areas, versus 20 W/m^2 through bare ice (red lines at $z = 0$, Figure 1c). If there was no horizontal redistribution of solar energy with depth, the absorption of solar radiation would also be partitioned between ponded and unponded regions at the same proportion. Instead, an average of 55 W/m^2 is absorbed in ocean points below melt ponds, and 45 W/m^2 is absorbed at ocean points below bare ice. In the case of Figure 1a, when taking into account the effect of pond geometry, the radiation absorbed in the upper ocean in regions underneath bare ice is more than doubled relative to if there was no horizontal redistribution (or a region of homogenous bare ice). The magnitude of these values scales with magnitude of solar forcing reaching the ice base (equation (2)). We next explore how this partitioning depends on pond geometry.

2.3. Fractal Geometry and the Pond Distribution Dimension

We next define a fractal-geometrical parameter that we call the "pond distribution dimension" (PDD) to characterize how melt water is distributed over the sea ice surface. In fractal geometry, the box-counting dimension, D_{bc}, is derived from the relationship between the number of boxes, n_i, of side length R_i that are necessary to cover the perimeter of a fractal region. Under the standard scaling assumption $n_i \sim R_i^{-D_{\mathrm{bc}}}$ as $i \to \infty$, the box-counting dimension is defined as

$$D_{\mathrm{bc}} = -\lim_{i\to\infty} \frac{\log n_i}{\log R_i}. \tag{3}$$

This can be discretely approximated by

$$D_{\mathrm{bc},i} = -\frac{\Delta \log n_i}{\Delta \log R_i}, \tag{4}$$

where $\Delta \log n_i = \log n_{i+1} - \log n_i$ and similarly for $\Delta \log R_i$. Pond surfaces do not exhibit scale invariance, so $D_{\mathrm{bc},i}$ is not constant.

We define the PDD as the average value of $D_{\mathrm{bc},i}$, weighted by the number of boxes of radius i,

$$\mathrm{PDD} = \frac{1}{\mathcal{N}} \sum_i n_i D_{\mathrm{bc},i} = \langle D_{\mathrm{bc},i} \rangle, \tag{5}$$

where $\mathcal{N} = \sum n_i$. This weighting emphasizes coverings by smaller box sizes (small i). Note that if $D_{\mathrm{bc},i}$ is constant, then PDD= D_{bc}.

While similar in form to traditional measures of two-dimensional geometry (Farmer, 1982), the newly defined PDD is distinct in that it is generally anticorrelated with increasing connectivity (Figures 3a–3c) and

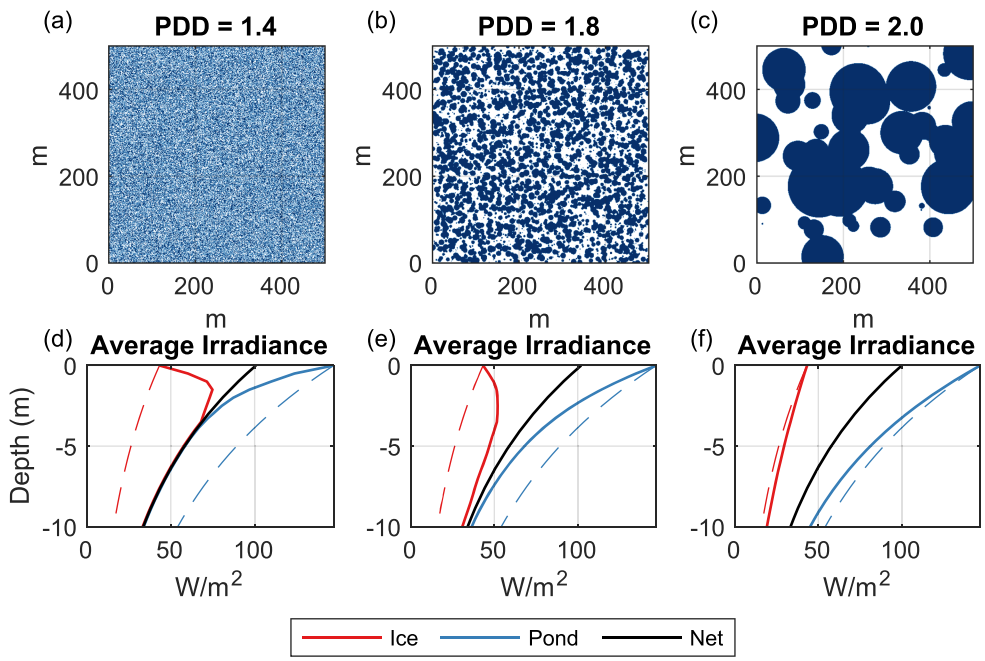

Figure 2. (a–c) Pond surfaces with melt pond fraction $\phi = 0.5$, with variable pond distribution dimension (PDD) of (a) 1.38, (b) 1.76, or (c) 1.96. Blue regions are ponded, white are unponded. (d–f) Average irradiance as a function of depth under bare ice (red), ponded ice (blue), or all ice regions (black) for the pond surfaces in (a–c). Dashed lines are the average irradiances under each surface type if the surface had only ponds (blue) or bare ice (red).

attains values less than 1 for isolated small ponds (Figure 2). Supporting information Figures S2 and S3a show that the PDD is poorly correlated with pond area, perimeter, box-counting dimension, or Hausdorff dimension but is related to the fraction of ponds that have a small area.

3. Results

We generate 5,000 square synthetic pond surfaces (as described in section 2), each 500×500 m^2 and characterized by a PDD obtained by varying r^* between 1 and 500 and ϕ^* between 0 and 1 (see acknowledgments for surfaces and light statistics). Figures 2a–2c show three example pond surfaces each with a melt pond fraction $\phi = 0.5$, for which the PDD ranges from 1.4 to 2. Figures 2d–2f show the average light field under all ponded (blue) or all unponded regions for the surfaces in Figures 2a–2c.

In the absence of lateral transmission of solar irradiance, the "predicted" solar flux to a region of ocean beneath ponded or bare ice is

$$I_{\mathrm{pred},p/i} = I_0(1 - \alpha_{p/i}) \exp(-\kappa_i h_i). \tag{6}$$

As we assume no scattering of solar energy within the water column, we may capture the isolated effect of pond geometry on the column-integrated light field. We define two "enhancement factors," $E_{p/i}$, equal to the percent change in solar absorption under ponded or pond-free regions relative to predicted exponential decay

$$E_{p/i} = \frac{I_{\mathrm{abs},p/i} - I_{\mathrm{pred},p/i}}{I_{\mathrm{pred},p/i}}, \tag{7}$$

where $I_{\mathrm{abs},p/i}$ is the total solar absorption in ocean columns underponds or bare ice and $I_{\mathrm{pred},ic}$ is the absorption assuming exponential extinction. A significant percentage of penetrating solar radiation is absorbed in pond-free regions, with the solar flux in these regions increased by 50% or more. Figure 3c shows the total change in heat flux absorbed in the ponded or unponded regions. Typical values of the heat flux, Q_{trans}, transferred between ponded and unponded regions are up to 15 W/m^2.

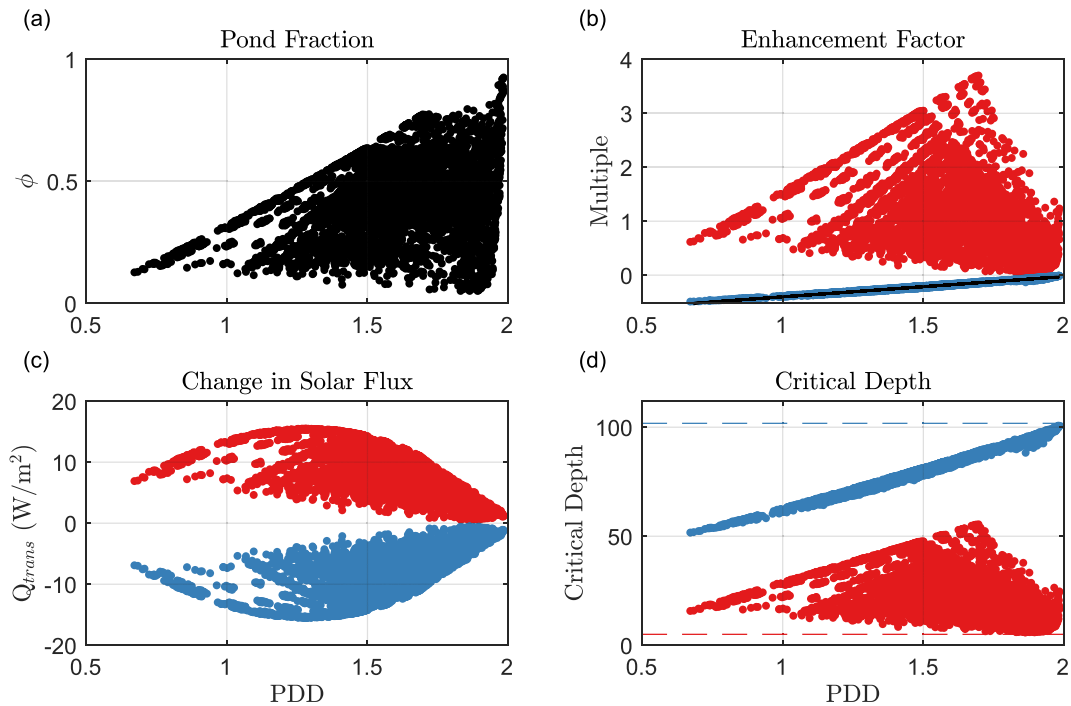

Figure 3. Relationship between under-ice light field and pond geometry for a collection of 5,000 stochastically generated melt pond surfaces. (a) Scatter plot of PDD against melt pond fraction, ϕ. (b) The "enhancement factor," $E_{p,i}$ in solar absorption for regions underponds (blue circles) or bare ice (red). The black line is a linear model (equation (8)) for E_p as a function of PDD. (c) The absolute change in solar heating Q_{trans} under ponded regions (blue) or pond-free regions (red), as a function of PDD. (d) Critical depth under ponded (blue) and unponded (red) surfaces) as a function of pond distribution dimension. Dashed lines are the critical depth for those regions when scattering at the ice-ocean interface is not included.

To determine quantitatively what controls the (negative) enhancement factor for ponded regions, we perform a multiple linear regression of E_p against three control variables: the pond fraction ϕ, the pond perimeter per area nondimensionalized by the attenuation coefficient, $\frac{P}{\kappa_w A}$ (where A is the total domain area), and PDD. The full regression accounts for nearly all the variance in E_p ($R^2 = .993$),

$$\tilde{E}_p = \left(-0.62 + 0.29\text{PDD} + 0.04\phi - 6 \times 10^{-3}\frac{P}{\kappa_w A}\right) \approx -0.6 + 0.3\text{PDD}. \tag{8}$$

Regressing on PDD alone compares favorably ($R^2 = 0.988$) to the full multilinear regression. Because E_p is a percentage change in irradiance, the weak relationship between E_p and ϕ is expected, as ϕ controls the magnitude of solar input. The weaker relationship between the (dimensionless) total pond perimeter per ice area $P/\kappa_w A$ and E_p is more surprising. In supporting information Figure S2 we show that perimeter-based metrics are weakly associated with E_p compared to PDD. In supporting information Figure S3b we show a potentially useful relationship between PDD and the fraction of ponds that have a small area, a metric that may be easier to observe than the PDD.

Inhomogeneous and anisotropic radiative transfer through sea ice affects the horizontal distribution of solar energy with depth, but it does not alter the domain-averaged downward solar flux at each depth, which follows Beer's law (see Figures 2d–2f). Thus, a relationship between the enhancement factor, E_i, for pond-free regions (red circles, Figure 3b) and PDD may be derived. Considering the partitioning of total solar energy as it decays with depth between under-ice and underpond regions,

$$E_i = -E_p \frac{I_{\text{pred},mp}}{I_{\text{pred},ic}}. \tag{9}$$

Noting that in our model of light transmission through ice,

$$\frac{I_{\text{pred},p}}{I_{\text{pred},ic}} = \frac{(1-\alpha_p)(\phi)}{(1-\alpha_i)(1-\phi)}, \tag{10}$$

we derive an expression for E_i,

$$E_i = -E_p \frac{\phi}{1-\phi} \frac{1-\alpha_p}{1-\alpha_i}. \tag{11}$$

Owing to the reciprocal in equation (11), the linear regression model fails when including values of ϕ approaching 1. Restricting to just the values of ϕ smaller than 0.7 (85% of the data set and accounting for almost all field observations), the linear model for E_i explains most of the variance in E_i ($R^2 = 0.975$). For clarity, the linear model for E_i is not shown in Figure 3b, as the fit is no longer a one-to-one function of PDD. A multiple linear regression E_i on the same variables used to derive equation (8) returns a model that explains less of the variance ($R^2 = 0.75$) than the nonlinear model of equation (11). We are therefore confident that the relation of equation (11) is appropriate, given the nearly linear scatter plot of E_p in Figure 3b.

Finally, Q_{trans}, the energy transferred from ponded to unponded regions due to light transmission through ice

$$\tilde{Q}_{\text{trans}}(\phi, \text{PDD}) = I_0 e^{-\kappa_i h} \phi (1-\alpha_p) \tilde{E}_p \approx I_0 e^{-\kappa_i h} \phi (1-\alpha_p)(0.3\text{PDD} - 0.6). \tag{12}$$

This model explains 89% of the variance in the value of Q_{trans} derived by integrating the explicitly computed light field (Figure 3c).

In summary, we determined a nearly linear relationship between E_p and PDD (Figure 3b), suggesting that the changing absorption of heat is controlled by the pond geometry. In supporting information Figure S4, we show that the linear relationship is robust, though its slope is affected by the dimensionless quantity $\kappa_w \Delta x$ and the attenuation coefficient of light in water multiplied by the minimum pond spacing Δx. The coefficient κ_w is a function of water mass properties such as biology or other contaminants in the upper ocean that increase solar absorption in the upper ocean (Bélanger et al., 2013) and alter the shape of the best fit line in Figure 3b. We do not find that changes to sea ice properties or ocean properties affect the linear relationship between E_p and *PDD* shown in Figure 3. Pond geometry affects the transfer of energy between ponded and unponded regions, and a larger value of PDD typically corresponds to well-separated ponds (Figure 2c), where the transfer of energy is small and the enhancement factor is close to zero. A smaller value of PDD (Figure 2a) corresponds to more connected geometry, more transfer of energy away from ponded regions, and a more negative enhancement factor E_p.

4. Implications

Here we have isolated the geometric effect that melt ponds may have on the instantaneous light field under sea ice. These instantaneous differences may have persistent effects, for example, on sub-ice ecological communities that travel with the ice and are exposed to the same light field over time or on ocean heating when relative ice-ocean velocities are small or where vertical mixing can homogenize lateral variations before horizontal mixing can eliminate them.

A common framework for understanding phytoplankton blooms is the "Sverdrup hypothesis" (Sverdrup, 1953), which theorizes that phytoplankton inhabit and are evenly mixed throughout the ocean surface mixed layer. When the mixed layer depth is shallower than a "critical depth," the average photosynthetically available radiation permits phytoplankton community growth and leads to blooms. Observations of "massive" phytoplankton blooms under fully ice-covered but ponded areas of the Chukchi Sea (Arrigo et al., 2012, 2014) have suggested that melt ponds are a significant factor.

Figure 3d uses the Sverdrup critical depth model for phytoplankton blooms under ponded sea ice derived in Horvat et al. (2017) to examine how changes to the pond surface geometry affect the potential for phytoplankton blooms. To do so, we assume that the differences between ponded and unponded regions remain fixed over the time for net primary production to begin, in general valid for weakly mixing regions, static sea ice, or for phytoplankton communities that travel with the ice. This assumption may be contrasted with the approach in Horvat et al. (2017), which assumed a horizontally homogenized light field over the scale of a single GCM grid cell. The critical depth is the deepest possible mixed layer that allows for net primary

production. In general, higher critical depths correspond to better light conditions for photosynthetic life. For purely homogeneous surfaces, ocean areas underponds (dashed blue line) permit blooms for mixed layers less than 101 m, typical for first-year ice regions in summer (Peralta-Ferriz & Woodgate, 2015). Thus, areas under ponded ice alone would be highly suitable to photosynthetic life. For ocean areas under bare ice (dashed red line) blooms are permitted only when the mixed layer is 5 m or less.

The under-ice light field homogenizes with increasing PDD. As PDD decreases, there is a linear decrease in irradiance under ponded regions (blue dots, Figure 2b), with less photosynthetically available radiation there. Ponded regions therefore become less hospitable, with the critical depth decreasing significantly, to as low as 57 m. Conversely, this leads to more hospitable conditions under bare ice, and the critical depth in those regions increases by a factor of up to 10 times as a function of PDD (red dots, Figure 3a).

Pond geometry may also feed back on sea ice evolution through the ocean heat flux if background ice-ocean relative motion is weak compared to the timescale for absorbed solar radiation to melt sea ice. Background under-ice vertical diffusivities in highly stratified under-ice boundary layers are ≈ 0.02 m^2/s (McPhee & Morison, 2001). Over a distance $\kappa_w^{-1} \approx 9$ m, this gives a timescale $\tau = \nu\kappa_w^2 \approx 1$ hr for vertical homogenization to turn the instantaneous effect of surface geometry to a persistent one. The corresponding ice-ocean speed difference to cover a 50-m wide melt pond is 1.5 cm/s (1.3 km/day), at the order of mean summer ice drift speeds (Kwok et al., 2013). We explored a simple parameterization of the effect of pond geometry on the distribution of under-ice solar fluxes in a standalone sea ice model, in which ocean-ice heat fluxes are redistributed between different ice thickness classes as a function of pond fraction (Text S1). We did not find a strong feedback on changes to sea ice thickness (Text S1 and Figure S5) in this preliminary effort. This is because the overall energy budget is unchanged, and feedbacks through changing the ice thickness distribution were relatively weak. Such thickness feedbacks should be reassessed in fully coupled biophysical models that permit the coupled evolution of light absorption, biology, the ocean mixed layer, and sea ice.

5. Conclusions

Here we have demonstrated the significant role that pond surface geometry can have on the instantaneous light field under sea ice. We found a metric, the PDD, that can be derived from the 2-D pond surface geometry and captures the horizontal partitioning of under-ice irradiance. The PDD cannot readily be derived in current climate models. Here we use synthetically generated ponds and can readily compute statistics of the ponded surface. Obtaining the same for real ponded ice surfaces and ice topographies will be an observational and modeling challenge. A first step may be to reprocess existing observations of melt ponds over sea ice (Hohenegger et al., 2012) to derive a seasonal cycle of PDD. Information about the real-world evolution of PDD during the melt season may help to fully understand the impact of melt ponds on Arctic climate, sea ice, and ecology.

We considered the instantaneous light field under ponded sea ice surfaces. To isolate the effect of pond geometry, we neglected scattering within the water column and variation in sea ice concentration, thickness, pond depth, or albedo, which all play a role in the distribution of solar energy with depth. Pond geometry can potentially play a role in persistent changes in under-ice heat and ecology. Interpreted as a heat flux, the variation in solar absorption under ponded and bare ice regions is also instantaneous, and its inhomogeneity could have a persistent effect when drift speeds are slow over short time periods. Many ecological communities experience a delay between solar energy absorption and net primary production (Lewis et al., 2019). Primary production is also nonlinearly related to solar energy input and other local factors (Boyd et al., 2013). Pond geometry is likely most important for ecological communities when horizontal ocean-ice motions are small or phytoplankton populations move with the ice. Further work using coupled biophysical models is required to assess the realistic impact of the effect isolated here in more detail.

Data Availability Statement

The generated synthetic pond surfaces used to produce the results, along with statistics of their light fields, are available as a PANGAEA data archive in compliance with FAIR Data Standards (http://doi.pangaea.de/10.1594/PANGAEA.908124). Code used to produce manuscript figures is available online (https://github.com/chhorvat/Melt-Pond-Light).

Acknowledgments
C. H. was supported by the NOAA Climate and Global Change Postdoctoral Fellowship Program, sponsored in part through cooperative Agreement NA16NWS4620043, Years 2017–2021, with the National Oceanic and Atmospheric Administration, U.S. Department of Commerce. K. M. G. acknowledges support from the the Applied and Computational Analysis Program and the Arctic and Global Prediction Program at the U. S. Office of Naval Research through Grants N00014-13-10291, N00014 -15-1-2455, N00014-18-1-2041, and N00014-18-1-2552, as well as support from the Division of Mathematical Sciences and the Division of Polar Programs at the U.S. National Science Foundation through Grants DMS-0940249, DMS-1413454, and DMS-1715680. L. R. was supported by Marsden Contract VUW 1408 and the Deep South National Science Challenge.The authors would like to thank the Isaac Newton Institute for Mathematical Sciences for support and hospitality during the programme "Mathematics of sea ice phenomena" when work on this paper was undertaken. This work was supported by EPSRC grant number EP/R014604/1".

References

Arrigo, K. R., Perovich, D. K., Pickart, R. S., Brown, Z. W., van Dijken, G. L., Lowry, K. E., & Swift, J. H. (2012). Massive phytoplankton blooms under Arctic Sea ice. *Science*, *336*(6087), 1408. https://doi.org/10.1126/science.1215065

Arrigo, K. R., Perovich, D. K., Pickart, R. S., Brown, Z. W., van Dijken, G. L., Lowry, K. E., & Swift, J. H. (2014). Phytoplankton blooms beneath the sea ice in the Chukchi sea. *Deep-Sea Research Part II: Topical Studies in Oceanography*, *105*, 1–16. https://doi.org/10.1016/j.dsr2.2014.03.018

Assmy, P., Fernández-Méndez, M., Duarte, P., Meyer, A., Randelhoff, A., Mundy, C. J., & Granskog, M. A. (2017). Leads in Arctic pack ice enable early phytoplankton blooms below snow-covered sea ice. *Scientific Reports*, *7*(1), 40850. https://doi.org/10.1038/srep40850

Bélanger, S., Babin, M., & Tremblay, J. E. J. É. (2013). Increasing cloudiness in Arctic damps the increase in phytoplankton primary production due to sea ice receding. *Biogeosciences*, *10*(6), 4087–4101. https://doi.org/10.5194/bg-10-4087-2013

Bowen, B., Strong, C., & Golden, K. M. (2018). Modeling the fractal geometry of Arctic melt ponds using the level sets of random surfaces. *Journal of Fractal Geometry*, *5*(2), 121–142.

Boyd, P. W., Rynearson, T. A., Armstrong, E. A., Fu, F., Hayashi, K., Hu, Z., & Thomas, M. K. (2013). *PLoS ONE*, *8*(5), e63091. https://doi.org/10.1371/journal.pone.0063091

Briegleb, B. P., & ight, B. (2007). A Delta-Eddington multiple scattering parameterization for solar radiation in the sea ice component of the Community Climate System Model (*Technical Note TN-472STR*): NCAR/TN-47, February, National Center for Atmospheric Research, National Center for Atmospheric Research, Boulder, CO, United States. https://doi.org/10.5065/D6B27S71

Cuevas, C. A., Maffezzoli, N., Corella, J. P., Spolaor, A., Vallelonga, P., Kjær, H. A., & Saiz-Lopez, A. (2018). Rapid increase in atmospheric iodine levels in the North Atlantic since the mid-20th century. *Nature Communications*, *9*(1), 1452. https://doi.org/10.1038/s41467-018-03756-1

Farmer, J. D. (1982). Information dimension and the probabilistic structure of chaos. *Zeitschrift für Naturforschung A*, *37*(11), 1304–1326. https://doi.org/10.1515/zna-1982-1117

Fetterer, F., & Untersteiner, N. (1998). Observations of melt ponds on Arctic sea ice. *Journal of Geophysical Research*, *103*(C11), 24,821–24,835. https://doi.org/10.1029/98JC02034

Frey, K. E., Perovich, D. K., & Light, B. (2011). The spatial distribution of solar radiation under a melting Arctic sea ice cover. *Geophysical Research Letters*, *38*, L22501. https://doi.org/10.1029/2011GL049421

Grenfell, T., Light, B., & Perovich, D. K. (2006). Spectral transmission and implications for the partitioning of shortwave radiation in Arctic sea ice. *Annals of Glaciology*, *44*, 1–6.

Grenfell, C., & Maykut, G. A. (1977). The optical properties of ice and snow in the Arctic Basin. *Journal of Glaciology*, *18*(80), 445–463. https://doi.org/10.1017/S0022143000021122

Hohenegger, C., Alali, B., Steffen, K. R., Perovich, D. K., & Golden, K. M. (2012). Transition in the fractal geometry of Arctic melt ponds. *Cryosphere*, *6*(5), 1157–1162. https://doi.org/10.5194/tc-6-1157-2012

Holland, M. M., Bailey, D. A., Briegleb, B. P., Light, B., & Hunke, E. (2012). Improved sea ice shortwave radiation physics in CCSM4: The impact of melt ponds and aerosols on Arctic sea ice. *Journal of Climate*, *25*(5), 1413–1430. https://doi.org/10.1175/JCLI-D-11-00078.1

Horvat, C., Jones, D. R., Iams, S., Schroeder, D., Flocco, D., & Feltham, D. (2017). The frequency and extent of sub-ice phytoplankton blooms in the Arctic Ocean. *Science Advances*, *3*(3), e1601191. https://doi.org/10.1126/sciadv.1601191

Huang, W., Lu, P., Lei, R., Xie, H., & Li, Z. (2016). Melt pond distribution and geometry in high Arctic sea ice derived from aerial investigations. *Annals of Glaciology*, *57*(73), 105–118. https://doi.org/10.1017/aog.2016.30

Kanamitsu, M., Ebisuzaki, W., Woollen, J., Yang, S. K., Hnilo, J. J., Fiorino, M., & Potter, G. L. (2002). NCEP-DOE AMIP-II reanalysis (R-2). *Bulletin of the American Meteorological Society*, *83*(11), 1631–1644. https://doi.org/10.1175/BAMS-83-11-1631(2002)083<1631:NAR>2.3.CO;2

Katlein, C., Nicolaus, M., & Petrich, C. (2014). The anisotropic scattering coefficient of sea ice. *Journal of Geophysical Research: Oceans*, *119*, 842–855. https://doi.org/10.1002/2013JC009502

Katlein, C., Perovich, D. K., & Nicolaus, M. (2016). Geometric effects of an inhomogeneous sea ice cover on the under ice light field. *Frontiers in Earth Science*, *4*(February), 2–11. https://doi.org/10.3389/feart.2016.00006

Kwok, R., Spreen, G., & Pang, S. (2013). Arctic sea ice circulation and drift speed: Decadal trends and ocean currents. *Journal of Geophysical Research: Oceans*, *118*, 2408–2425. https://doi.org/10.1002/jgrc.20191

Laney, S. R., Krishfield, R. A., & Toole, J. M. (2017). The euphotic zone under Arctic Ocean sea ice: Vertical extents and seasonal trends. *Limnology and Oceanography*, *62*(5), 1910–1934. https://doi.org/10.1002/lno.10543

Laney, S. R., Krishfield, R. A., Toole, J. M., Hammar, T. R., Ashjian, C. J., & Timmermans, M. L. (2014). Assessing algal biomass and bio-optical distributions in perennially ice-covered polar ocean ecosystems. *Polar Science*, *8*(2), 73–85. https://doi.org/10.1016/j.polar.2013.12.003

Langleben, M. P. (1969). Albedo and degree of puddling of a melting cover of sea ice. *Journal of Glaciology*, *8*(54), 407–412. https://doi.org/10.1017/S002214300002699X

Lenoble, J. (1985). *Radiative transfer in scattering and absorbing atmospheres: Standard computational procedures*, pp. 314. Hampton, VA: A. Deepak Publishing, 1985.

Lewis, K. M., Arntsen, A. E., Coupel, P., Joy-Warren, H., Lowry, K. E., Matsuoka, A., & Arrigo, K. R. (2019). Photoacclimation of Arctic Ocean phytoplankton to shifting light and nutrient limitation. *Limnology and Oceanography*, *64*(1), 284–301. https://doi.org/10.1002/lno.11039

Light, B., Grenfell, T. C., & Perovich, D. K. (2008). Transmission and absorption of solar radiation by Arctic sea ice during the melt season. *Journal of Geophysical Research*, *113*, C03023. https://doi.org/10.1029/2006JC003977

Light, B., Perovich, D. K., Webster, M. A., Polashenski, C., & Dadic, R. (2015). Optical properties of melting first-year Arctic sea ice. *Journal of Geophysical Research: Oceans*, *120*, 7657–7675. https://doi.org/10.1002/2015JC011163

Lu, P., Li, Z. J., Zhang, Z. H., & Dong, X. L. (2008). Aerial observations of floe size distribution in the marginal ice zone of summer Prydz Bay. *Journal of Geophysical Research*, *113*, C02011. https://doi.org/10.1029/2006JC003965

Ma, Y. P., Sudakov, I., Strong, C., & Golden, K. M. (2019). Ising model for melt ponds on Arctic sea ice. *New Journal of Physics*, *21*(6), 063029. https://doi.org/10.1088/1367-2630/ab26db

McPhee, M. G., & Morison, J. H. (2001). Under-ice boundary layer, *Encyclopedia of Ocean Sciences* (pp. 3071–3078), Elsevier. ISBN: 0-12-227430-X. https://doi.org/10.1006/rwos.2001.0146

Mundy, C. J., Gosselin, M., Ehn, J., Gratton, Y., Rossnagel, A., Barber, D. G., & Papakyriakou, T. (2009). Contribution of under-ice primary production to an ice-edge upwelling phytoplankton bloom in the Canadian Beaufort Sea. *Geophysical Research Letters*, *36*, L17601. https://doi.org/10.1029/2009GL038837

Nicolaus, M., Katlein, C., Maslanik, J., & Hendricks, S. (2012). Changes in Arctic sea ice result in increasing light transmittance and absorption. *Geophysical Research Letters*, *39*, 2012GL053738. https://doi.org/10.1029/2012GL053738

Ordóñez, C., Lamarque, J. F., Tilmes, S., Kinnison, D. E., Atlas, E. L., Blake, D. R., & Saiz-Lopez, A. (2012). Bromine and iodine chemistry in a global chemistry-climate model: Description and evaluation of very short-lived oceanic sources. *Atmospheric Chemistry and Physics*, *12*(3), 1423–1447. https://doi.org/10.5194/acp-12-1423-2012

Peralta-Ferriz, C., & Woodgate, R. A. (2015). Seasonal and interannual variability of pan-Arctic surface mixed layer properties from 1979 to 2012 from hydrographic data, and the dominance of stratification for multiyear mixed layer depth shoaling. *Progress in Oceanography*, *134*, 19–53. https://doi.org/10.1016/j.pocean.2014.12.005

Perovich, D. K., Light, B., Eicken, H., Jones, K. F., Runciman, K., & Nghiem, S. V. (2007). Increasing solar heating of the Arctic Ocean and adjacent seas, 1979-2005: Attribution and role in the ice-albedo feedback. *Geophysical Research Letters*, *34*, L19505. https://doi.org/10.1029/2007GL031480

Perovich, D. K., Nghiem, S. V., Markus, T., & Schweiger, A. (2007). Seasonal evolution and interannual variability of the local solar energy absorbed by the Arctic sea ice-ocean system. *Journal of Geophysical Research*, *112*, C03005. https://doi.org/10.1029/2006JC003558

Perovich, D. K., & Richter-Menge, J. a. (2009). Loss of sea ice in the Arctic. *Annual Review of Marine Science*, *1*(1), 417–441. https://doi.org/10.1146/annurev.marine.010908.163805

Polashenski, C., Golden, K. M., Perovich, D. K., Skyllingstad, E., Arnsten, A., Stwertka, C., & Wright, N. (2017). Percolation blockage: A process that enables melt pond formation on first year Arctic sea ice. *Journal of Geophysical Research: Oceans*, *122*, 413–440. https://doi.org/10.1002/2016JC011994

Polashenski, C., Perovich, D., & Courville, Z. (2012). The mechanisms of sea ice melt pond formation and evolution. *Journal of Geophysical Research*, *117*, C01001. https://doi.org/10.1029/2011JC007231

Popović, P., Cael, B. B., Silber, M., & Abbot, D. S. (2018). Simple rules govern the patterns of Arctic sea ice melt ponds. *Physical Review Letters*, *120*(14), 148701. https://doi.org/10.1103/PhysRevLett.120.148701

Rösel, A., Kaleschke, L., & Birnbaum, G. (2012). Melt ponds on Arctic sea ice determined from MODIS satellite data using an artificial neural network. *The Cryosphere*, *6*(2), 431–446. https://doi.org/10.5194/tc-6-431-2012

Schröder, D., Feltham, D. L., Flocco, D., & Tsamados, M. (2014). September Arctic sea-ice minimum predicted by spring melt-pond fraction. *Nature Climate Change*, *4*(5), 353–357. https://doi.org/10.1038/nclimate2203

Stroeve, J. C., Markus, T., Boisvert, L., Miller, J., & Barrett, A. (2014). Changes in Arctic melt season and implications for sea ice loss. *Geophysical Research Letters*, *41*, 1216–1225. https://doi.org/10.1002/2013GL058951

Sverdrup, H. U. (1953). On conditions for the vernal blooming of phytoplankton. *ICES Journal of Marine Science*, *18*(3), 287–295. https://doi.org/10.1093/icesjms/18.3.287

Taskjelle, T., Hudson, S. R., Granskog, M. A., & Hamre, B. (2017). Modelling radiative transfer through ponded first-year Arctic sea ice with a plane-parallel model. *Cryosphere*, *11*(5), 2137–2148. https://doi.org/10.5194/tc-11-2137-2017

Trodahl, H. J., Buckley, R. G., & Brown, S. (1987). Diffusive transport of light in sea ice. *Applied Optics*, *26*(15), 3005. https://doi.org/10.1364/AO.26.003005

Vihma, T. (2014). Effects of Arctic sea ice decline on weather and climate: A review. *Surveys in Geophysics*, *35*(5), 1175–1214. https://doi.org/10.1007/s10712-014-9284-0